https://doi.org/10.1016/j.joule.2021.05.010

This is the Pre-Published Version.

Integrated Solar-driven PV Cooling and Seawater Desalination with Zero Liquid Discharge

Wenbin Wang,[1, 3] Sara Aleid,[1, 3] Yifeng Shi,[1] Chenlin Zhang,[1] Renyuan Li,[1] Mengchun Wu,[1] Sifei Zhuo[1], Peng Wang[1, 2,4, *]

[1]Water Desalination and Reuse Center, Division of Biological and Environmental Science and Engineering, King Abdullah University of Science and Technology, Thuwal 23955-6900, Saudi Arabia.

[2]Hong Kong Polytechnic University, Hung Hom, Kowloon, Hong Kong, China.

[3]These authors contributed equally.

[4]Lead Contact.

[*]Correspondence: peng.wang@kaust.edu.sa (P.W.).

SUMMARY

Utilizing the "waste heat" of solar cell for desalination enables a simultaneous production of freshwater and electricity in an inexpensive manner and thus represents low barrier-of-entry electricity and freshwater supplies suitable to off-grid communities for point-of-consumption. Thus, its adoption can facilitate the obtainment of the United Nation's Sustainable Development 6th and 7th Goals (SDG6 and SDG7) by 2030. Especially, in such a design, the freshwater production performance can be significantly increased via recycling the latent heat of vapor condensation by multistage membrane distillation (MSMD). Nevertheless, all previous works had to strike a delicate balance between temperature of the solar cell and freshwater production rate. Additionally, the desalination performance of MSMD was rarely evaluated by real seawater and the treatment of the produced concentrated brine during desalination still remains hugely challenging. Herein, guided by the theoretical modelling, this project demonstrated, for the first time, that a higher freshwater production rate and a lower solar cell temperature could indeed

© 2021. This manuscript version is made available under the CC-BY-NC-ND 4.0 license https://creativecommons.org/licenses/by-nc-nd/4.0/

be achieved at the same time, which represents a significant advancement. With a 5-stage photovoltaics-MSMD-evaporative crystallizer (PME) device, this project experimentally demonstrated a high and stable freshwater production rate of ~2.45 kg m^{-2} h^{-1} for real seawater desalination and a reduced solar cell temperature of ~47°C under one-sun irradiation in lab conditions, as compared to ~62°C of the same solar cell working alone. The reduced solar cell temperature led to an 8% increase in its electricity production. Moreover, the concentrated brine produced in the process was fully evaporated by the underlying evaporative crystallizer, achieving zero liquid discharge (ZLD) for the entire system. The results of this work would benefit the general MSMD design for water treatment utilizing low-grade heat.

Keywords: solar cell, solar desalination, zero liquid discharge, water-energy nexus, solar cell cooling, vaporization enthalpy recycling.

Context & Scale

The simultaneous production of freshwater and electricity from solar energy is emerging as a feasible strategy to manage the water-energy nexus. To date, a multitude of technologies have been proposed and among them, the utilization of waste heat of solar cell for desalination shows a great promise. However, in such a design, a high clean water production performance is generally at the expense of a high solar cell temperature, which unproductively results in a low electricity generation efficiency. This work develops a photovoltaics-multistage membrane distillation-evaporative crystallizer (PME), which achieves efficient seawater desalination, electricity generation, PV cooling as well as zero liquid discharge within one device. The solar cell in PME shows an increased electricity generation efficiency owing to the reduced temperature. Importantly, PME delivers a successful performance with real red seawater as feed, proving its potential in practical application. This work provides a promising solution to produce low barrier-of-entry electricity and freshwater which is suitable to off-grid communities for point-of-consumption.

INTRODUCTION

There is nothing more essential to our daily life than water. It was estimated that about 785 million people around the globe who still do not have even a basic daily access to safe drinking water, which results in more than 200 million human hours spent every day mostly by women and girls to fetch drinking water for their families, a primitive and very ineffective use of human time.[1-6] In the regions with poor economic conditions, freshwater scarcity is tightly linked to their lack of energy, especially in the form of electricity, as any sufficient water treatment process consumes energy.[7-10] Up to now, annual electricity consumption in 36 countries is below 200 kWh per capita where understandably a large portion of the population is under severe freshwater scarcity while it is more than 11,000 kWh per capita in many developed countries.[11]

On the other hand, the alarming level of increasing frequency of extreme weather conditions across the globe alerts the world to curb its CO_2 emission significantly and do it quickly while the steadily improved life standards, increasing population, and industrialization of the underdeveloped economies all demand more energy, especially electricity, to be generated in the years to come.[12-14] This dilemma can only be bridged by non-fossil fuels energy source, among which photovoltaics (PV) distinguishes itself as arguably the most promising one due to its very low carbon footprint, technology maturity, and low barrier of entry.[15; 16] It is predicted by the European Union's (EU) photovoltaics status report that global PV installation capacity will increase to 1500 GW by 2025 and to more than 3000 GW by 2030.[17]

Nonetheless, the solar-to-electricity conversion efficiency of single-junction solar cell-based PV panels is constrained to 33.3% based on Shockley Quisser limit.[18] In practice, commercial PV panels convert no more than 25% of the absorbed solar energy to electricity.[19] The remaining absorbed solar energy is converted into heat and unproductively dumped as waste into the ambient surroundings, leading to a high PV panel temperature due to the inefficient thermal dissipation. In arid and semi-arid regions, the PV panels can be heated up to as high as 40^{o}C above the ambient air during daytime, which is detrimental to electricity generation and lifespan of the panels.[20; 21] It has been reported that an increased cell temperature results in a decline in its open circuit voltage (V_{oc}), fill factor and power output at rates of 2-2.3 mV $^{o}C^{-1}$, 0.1-0.2% $^{o}C^{-1}$ and 0.4-

0.5% $^{o}C^{-1}$, respectively.[22-25] Furthermore, every 10 ^{o}C temperature rise leads to a doubled panel aging rate.[26] Therefore, effective cooling to lower the solar cell's temperature will be a meaningful and significant contribution at the global renewable energy.

In this work, we report a photovoltaics-membrane distillation-evaporative crystallizer device (PME), as shown in Figure 1, which is capable of reducing the solar cell temperature by over 10^{o}C and, at the same time, continuously producing freshwater at a very high rate. In achieving so, the PME system generates no waste brine and thus obtains a simultaneous PV cooling and desalination with zero liquid discharge.

In the PME system, the multi-stage membrane distillation (MSMD) component is integrated on the backside of the solar cell and utilizes the waste heat of the solar cell directly to drive water evaporation. The design of the MSMD allows for collection and reuse of the latent heat of vapor condensation in each distillation stage to drive water evaporation of next stage.[27] Importantly, an evaporative crystallizer (EC) is designed to utilize the low-grade latent heat of the vapor condensation in the last stage of the MSMD to drive the evaporation of the concentrated brine produced in the previous stages. The end-product of the EC is the crystallized salt solid, leading to zero liquid discharge (ZLD) of the entire system. A theoretical model is developed to simulate the heat and mass flow within the PME and the modeling results point to the hydrophobic membranes in the MSMD component as the key to the goal of the simultaneous PV cooling and high water production rate within such a design.

In our previous work, we reported the first design of photovoltaics-membrane distillation device (PV-MD) with a cross-flow scheme, which produced a clean water production rate at 1.64 kg m^{-2} h^{-1} when using seawater as feedwater.[19] However, PV-cooling effect was not achieved and a relatively high solar cell temperature of ~58^{o}C persisted under one sun illumination in lab conditions in the previous PV-MD. In another recent work, a device similar to the PV-MD but with a dead-end flow design was used and showed a water production rate of 1.11 kg m^{-2} h^{-1} with a solar cell temperature of 50.2^{o}C under one sun illumination in lab conditions.[19] However, the dead-end flow design in this work leads to serious salt accumulation inside the device, which makes it unfeasible in practical applications and, at the same time, complicates a reliable data

interpretation. Besides, Zhu's group reported a hybrid tandem device constructed by integrating a reduced graphene oxide (r-GO)-based solar water purifier under a solar cell, which produced a water production rate of 0.80 kg m^{-2} h^{-1} with a solar cell temperature of around 39 ^{o}C.[28] As seen, the previous attempts all were not successful to achieve simultaneous improvement on both PV cell cooling and water production performance and such a solution to doing so remains elusive.

Herein, guided by the modeling results, a hydrophobic membrane with a thickness of 0.1 mm and porosity of 0.86 was rationally selected to fabricate a 5-stage PME device. Under one sun illumination in lab conditions with a room temperature of ~24^{o}C, the PME device was able to reduce the temperature of the solar cell to 46.6~47.8^{o}C, as compared to ~61.2^{o}C of the same solar cell working alone. The solar cell, due to its lower temperature in the PME, in turn, produced nearly 8% more electricity under the otherwise the same conditions. Amazingly, under the same lab conditions, the same PME produced freshwater from seawater at a rate of 2.35~2.45 kg m^{-2} h^{-1}, which almost doubles those previously reported in the literature. Furthermore, the concentrated brine evaporation rate, denoted as the brine treatment capacity hereafter, of the EC was controlled to be higher than the production rate of the concentrated brine of the MSMD, making the entire clean water production a ZLD process. The practical performance of the PME was confirmed by conducting outdoor experiments in field conditions. This work achieves a higher water production rate at a lower solar cell temperature, which represents a significant advancement in the field of solar driven simultaneous electricity and freshwater production. It has a potential to make a meaningful contribution to the global water-energy-climate nexus and facilitate the obtainment of the United Nation's Sustainable Development 6th and 7th Goals (SDG6 and SDG7) as it provides a promising solution to low barrier-of-entry electricity and freshwater supplies suitable to off-grid communities for point-of-consumption.[29; 30]

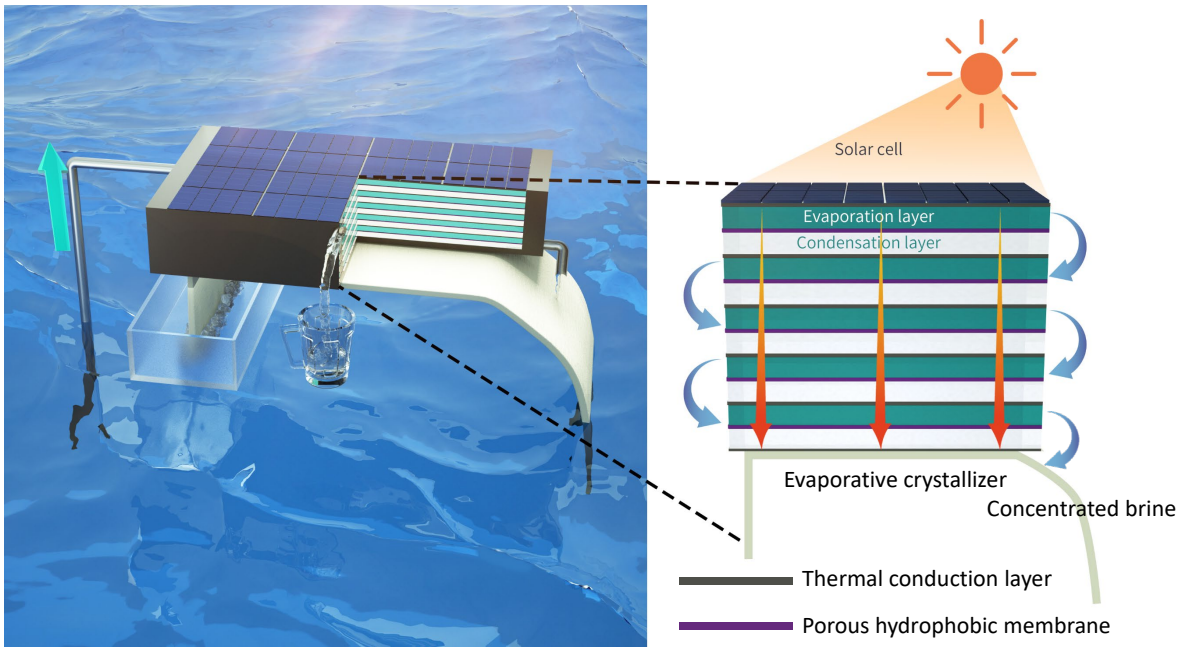

Figure 1. Schematic illustration of the integrated photovoltaics-membrane distillation-evaporative crystallizer (PME) device.

RESULTS

Design of the PME.

The overall design of the PME device is depicted in Figure 1. As seen, the solar energy is absorbed by the solar cell on the top and converted into electricity and heat. A multistage membrane distillation (MSMD) component is placed seamlessly on the backside of the solar cell. Each stage of the MSMD consists of 4 parts: a thermal conduction layer, an evaporation layer, a hydrophobic membrane, and a condensation layer. During the operation, feedwater (e.g., seawater) flows into the evaporation layer and some gets evaporated there driven by the heat generated from the solar cell (in the first stage) or the latent heat released by the vapor condensation in the immediately previous stage (in the stages other than the first one). The heat is conducted to the evaporation layer via the conduction layer. The generated vapor passes through the porous hydrophobic membrane and then gets condensed in the condensation layer to produce freshwater. This evaporation-condensation process is governed by the vapor pressure gradient between the evaporation layer and condensation layer within each stage, which is dictated by

their temperature disparity. To avoid the crystallization and accumulation of solid salt inside the evaporation layer and thus to have a stable operation, a crossflow mode is necessary, as shown in Figure S1. When water is being evaporated, the feedwater gets concentrated in the course of moving through the evaporation layer, the crossflow mode makes sure the concentrated feedwater, termed as concentrated brine in this work, exits the device before reaching its salt saturation. The concentrated brine is then wicked into the porous non-woven fabrics of the EC where it gets evaporated into the ambient. The EC is directly on the backside of the last MSMD stage where it facilitates the dissipation of the low-grade latent heat produced by the water vapor condensation in the last stage and at the same time turns the waste brine into crystallized salt solid. The treatment capacity of the EC is designed to be higher than the concentrated brine discharge rate by the MSMD, making the entire PME system to achieve an obvious zero liquid discharge.

Model simulation and membrane screening. From a theoretical point of view, in such a design, adding more stages can certainly increase the water production rate, but a higher solar cell temperature would be resulted in due to the increased thermal resistance. On the other hand, reducing the thickness of the hydrophobic membrane would decrease the vapor diffusion resistance, but reduce the temperature difference between the evaporation layer and condensation layer in the same stage, which is the driving force behind the vapor mass flux. In addition, increasing the porosity and pore size of the hydrophobic membrane can reduce the vapor diffusion resistance, thus rendering a higher water production rate, but their effects on the solar cell temperature remain unclear and call for further investigation. These dilemmas make the optimization direction of each parameter of each component not a simple choice. Therefore, we developed a thermal model to ascertain the roles of these parameters in determining both cell temperature and water production rate and to further identify the optimized ones for PME (the details of the theoretical model setup are presented in Note S1).[5; 31-36]

The results of the modeling indicate that both the water production performance and the solar cell temperature are greatly affected by the thickness of the hydrophobic membrane (δ) (Figure S2 A-B), with a smaller thickness leading to a higher water production rate and lower solar cell temperature. The membrane porosity has a significant effect on the water production rate but

little effect on the solar cell temperature (Figure S2 C-D), with a larger porosity reducing the solar cell temperature slightly while increasing the water production rate considerably. When the pore size is smaller than the mean free path of vapor (0.13 μm)[37], it shows a clear effect on the water production rate and solar cell temperature, with an increasing pore size resulting in a higher water production rate and lower solar cell temperature (Figure S1 E-F). When the pore size is slightly higher than the mean free path of vapor, a steep drop in the water production rate and a sharp increase in solar cell temperature are observed. Further increasing the pore size only slightly increases water production rate and decreases solar cell temperature. More details will be presented later in the discussion section. As a result, in this work, we chose a commercial polytetrafluoroethylene (PTFE) hydrophobic membrane with the thickness of 0.1 mm, porosity of 0.86, and pore size of 1.0 μm. It is worth pointing out that, based on the simulation results, the optimized membrane pore size should be slightly lower than the mean free path of vapor (0.13 μm). Since even a slight change in the pore size around 0.13 μm would greatly affect both clean water production rate and solar cell temperature, the pore size needs to be controlled in a very narrow region, which is technically challenging. Instead, with other factors being considered, the hydrophobic membrane with the pore size of 1.0 μm was chosen, because, compared to the optimized pore size of 0.13 μm, it reduces the water production rate by only ~3% and increases the solar cell temperature by only around ~1^{o}C. As a proof-of-concept, 5 stage MSMD component was employed to strike a good balance between the water production rate and solar cell temperature in this work.

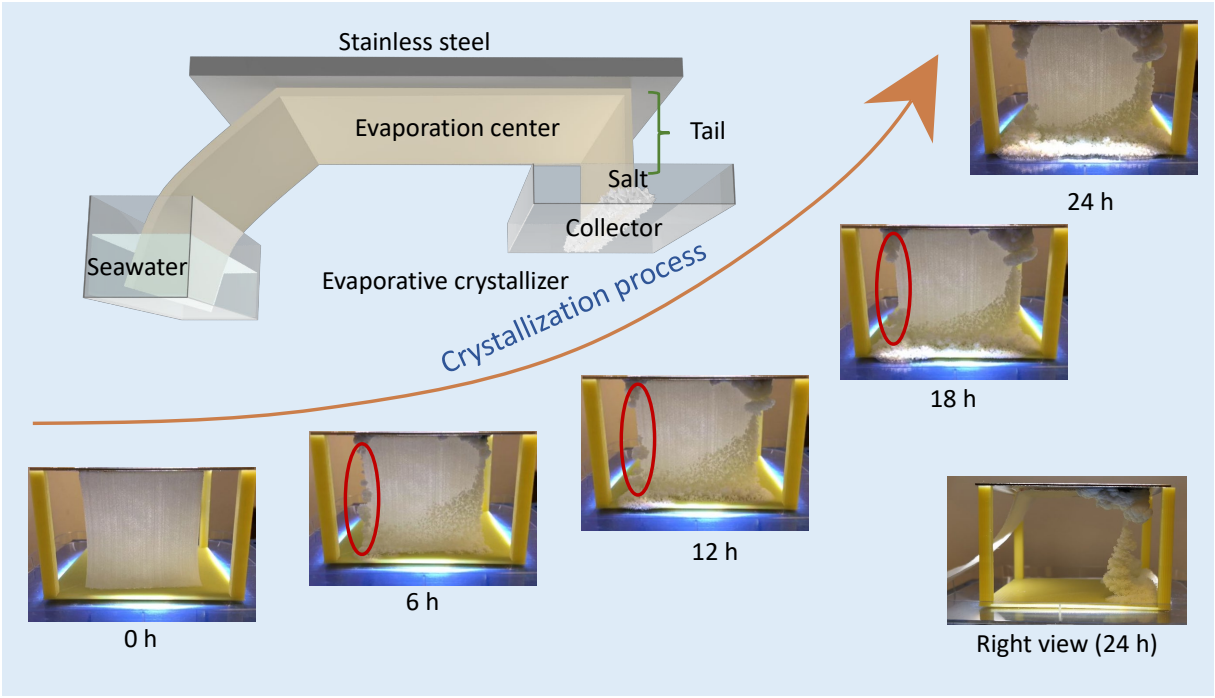

Figure 2. Schematic illustration of the evaporative crystallizer (EC) and the salt crystallization process in the EC.

Design of the Evaporative Crystallizer. The EC was made by non-woven fabrics, with its central part adhering directly underneath the bottom of the MSMD component and its tail part unattached (Figure 2 and Figure S3). The source brine is wicked by and transported along the fabrics all the way to the end of the tail part driven by a combined capillary and transpiration effect. Due to edge preferential crystallization, the salt is accumulated dominantly on the tail part of the fabrics, which simplifies salt collection.[38] It has been shown that interfacial evaporation of real seawater on a porous substrate would have a salt scaling issue which leads to the blockage of the porous material, resulting in a reduced treatment capacity and ultimate system failure (See more details in Figure S4 and Note S2).[39] In this work, a small amount of nitrilotriacetic acid (NTA) (10 ppm), which is nontoxic and biodegradable, was added into the real seawater to prevent the salt crystals from blocking.[39-41] The EC exhibited a stable brine treatment capacity in this work (see more details in Figure S4 and Note S2).

As shown in Figure 2, after 6 hours illumination at one sun (1000 W m^{-2}) in lab conditions, the salt started to accumulate on the tail. At the 12th hour, there was more salt on the tail and some

salt accumulation appeared on the joint between the EC center and tail. Importantly, the crystallized salt could fall off EC autonomously under its own gravity as evidenced by the disappearance of the salt solids in the marked area from 6 h to 18 h. In the next 18 hours (7th to 24th hours), the crystallized salts on the container floor underneath the tail were increasingly accumulating, indicating a self-sustained salt self-cleaning of the EC. A cross view clearly shows that most of the salts were accumulated near the tail part of the EC (See more details in Note S3).

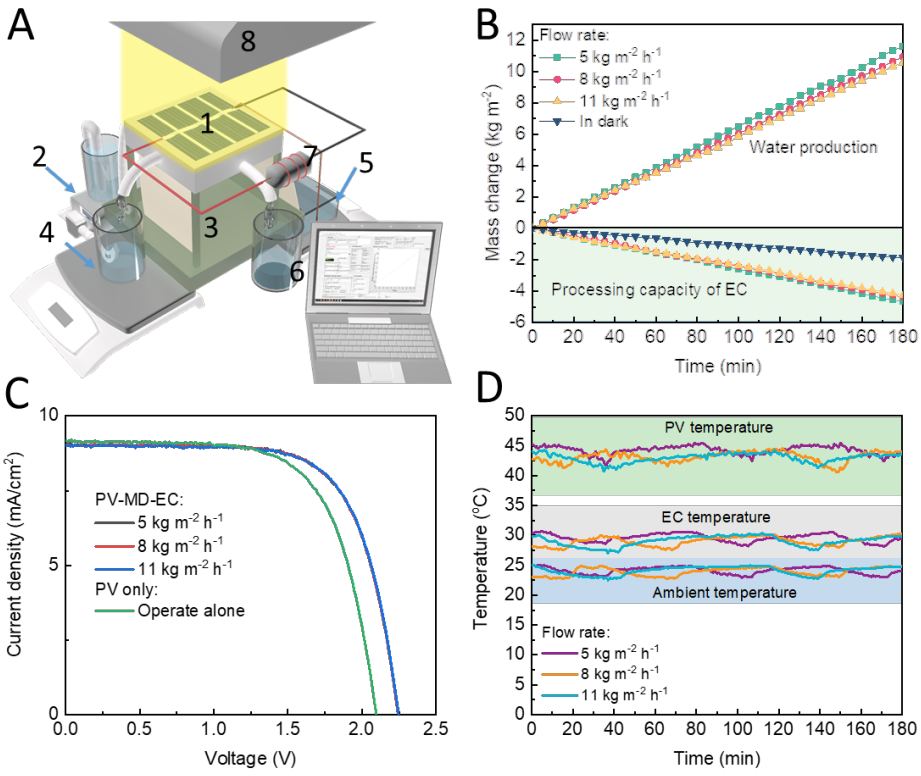

Figure 3. Water production and electricity generation evaluation of PME. (A) Experimental setup (1 PME device, 2 feedwater container and pump, 3 evaporative crystallizer (EC) and salt collector, 4 freshwater collector and electrical balance, 5 source water container of EC and electrical balance, 6 concentrated brine collector and computer, 7 resistance and thermal couple, 8 solar simulator). (B) The water production and treatment capacity of the PME under one sun illumination. (C) J-V curve of the solar cell in PME system at different feedwater flow rates. (D) The temperature profile. Note: having the source water container of EC (5) is for the purpose of continuously monitoring brine treatment capacity of EC.

Simultaneous production of freshwater and electricity. The freshwater production performance, solar cell temperature and electricity conversion efficiency of the PME system were firstly evaluated in a lab-made experimental setup (Figure 3a and Figure S5a) with pure water as feedwater. A mechanical pump was used for piping the source feedwater into the device. The solar cell was connected to a 15 Ω resistor, allowing a maximum power output of the solar cell. Additionally, the J-V curve of the solar cell was measured by connecting the solar cell to a Keithley 2400 series source meter. The solar absorptance of the solar cell, which is used to estimate the ability of the solar cell to harvest sunlight as solar spectrum is not uniformly distributed, was calculated to be 0.89 (Figure S5b and Supplementary Note S4)[42], indicating that 89% of solar energy can be harvested by the solar cell. When the flow rate of the feedwater was 5 kg m^{-2} h^{-1}, the PME device exhibited a water production rate of 3.85 kg m^{-2} h^{-1} and the treatment capacity of the EC was measured to be 1.54 kg m^{-2} h^{-1}. In this case, it can be calculated that the flow rate of the water that flows out of the device's evaporation layers combined was 1.15 kg m^{-2} h^{-1}, which is lower than the treatment capacity of EC, implying that zero liquid discharge can be achieved. In addition, the treatment capacity of the EC in dark reached up to 0.63 kg m^{-2} h^{-1}due to continuous water evaporation by EC.

When the feedwater flow rate was increased to 8 and 11 kg m^{-2} h^{-1}, the water production rate was decreased to 3.67 and 3.51 kg m^{-2} h^{-1}, respectively. The treatment capacity of EC was 1.47 and 1.38 kg m^{-2} h^{-1} for these two cases, respectively. These results indicate that the water production rate is only slightly affected by the feedwater flow rates, which can be attributed to the much lower specific heat of water (~4.2 kJ kg^{-1} K^{-1}) compared to its latent heat (~2257 kJ kg^{-1}).

When the solar cell was working alone, it exhibited a temperature of around 61.2°C (Figure S6) with an electricity conversion efficiency (defined as the percentage of the incoming solar radiation energy that is converted into electricity[43]) of 12.9% (Figure 3c). For the same solar cell in the PME device, its temperature at the feedwater flow rate of 5, 8 and 11 kg m^{-2} h^{-1} were measured to be 44.3, 43.1 and 42.9°C (Figure 3d), respectively, much lower than that of the solar cell working alone (i.e., 61.2°C) and the conventional PV-MD device (~58°C) as reported previously. It has to be pointed out that all these experiments were conducted at a constant

ambient temperature of ~24°C and relative humidity of ~60%. In addition, the temperature of the EC was only 5°C higher than ambient temperature due to its high water treatment capacity. The electricity conversion efficiency under these three feedwater flow rates were increased to be between 14.0~14.2% due to the reduced temperature of the solar cell. These results demonstrate that the PME device can achieve a higher clean water production rate with a simultaneous lower solar cell temperature and, more importantly, produce 8% more electricity than the same solar cell alone. By controlling the flow rate of the feedwater, zero liquid discharge can be achieved.

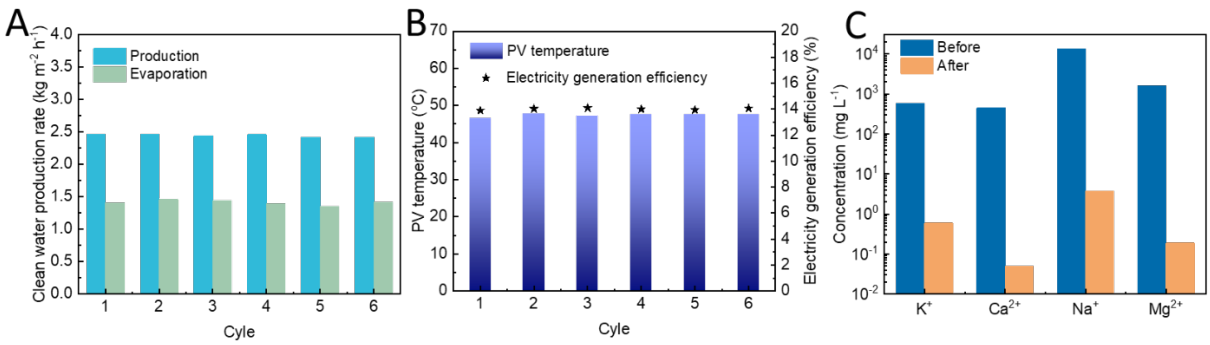

Figure 4. Durability evaluation of PME. (A) Water production rate and concentrated brine treatment capacity in different cycle. (B) Temperature and electricity conversion efficiency of the PV. (C) Salinity of the feedwater and produced freshwater.

Seawater desalination. One of the main targeted applications of the PME system is to desalinate seawater. Therefore, the real seawater (from Red Sea) was directly used as feedwater and six daily cycles were conducted to investigate the performance stability of the system. Before desalination, the scale inhibitor (5 ppm) and NTA (10 ppm) were added into the seawater. The scale inhibitor is to minimize the scaling forming inside MSMD while NTA is to prevent salt crystals from blocking the fabrics of the EC.

Considering that the brine treatment capacity of the EC is higher than the concentrated brine discharge rate, certain amount of seawater was added to the concentrated brine container before water evaporation on EC to ensure a continuous operation (namely making sure that EC would not go completely dry). The solar cell was connected to a 15 Ω resistor as an output load.

To realize ZLD, the flow rate of the seawater was controlled by a mechanical pump at 3.50 kg m^{-2} h^{-1} during the experiment. The PME device was irradiated under one sun irradiation continuously for 8 hours of each cycle, as shown in Figure 4. Throughout the six cycles, the PME showed an uncompromised water production rate at the range of 2.35~2.45 kg m^{-2} h^{-1} and brine treatment capacity of 1.30~1.45 kg m^{-2} h^{-1}. Moreover, the porosity of the hydrophobic membrane in each stage was measured after 6 cycles to further investigate the membrane scaling. As shown in Figure S7, the porosity of the 5 pieces of hydrophobic membrane were at around ~0.86, which are comparable to the unused membrane, indicating an excellent anti-scaling performance. The PV exhibited reduced temperature at 46.6~47.8ºC, and increased electricity conversion efficiency at 13.9~14.0% accordingly, representing around an 8% increase in electricity generation. These results demonstrate that the PME system has good durability and stability. However, these performance values are a bit lower than the ones with the pure water as feedwater due to the lower saturated vapor pressure of seawater.

To demonstrate that our system is capable of working in a passive manner, we further developed a gravity-driven water delivery mode. A medical infusion set-like system (Figure S8 and S9A-B) was designed in which the container was sealed by a lid and an air filter was added at the outlet of the container. In such a system, when the water flows out, the air pressure above the liquid would be reduced, which drives the air to flow into the sealed container via the air filter and helps maintain the system at a constant pressure (See more details in Note S5). To investigate the effect of the water level, a bottle with a volume of 500 ml and diameter of 7 cm was used as the feedwater container and the initial flow rate was modulated to be around 20 g min^{-1}. As shown in Figure S9D and E, the system with an air filter exhibited a stable flow rate while the system without an air filter showed a monotonically reduced flow rate. It can be calculated that the height of the water level was reduced by 6.8 and 10.4 cm in the bottle without and with an air filter, respectively, indicating that the water level inside the bottle has little effect on the flow rate in the system with an air filter. Under one-sun illumination, the PME with the gravity-driven water flow mode delivered a clean water production rate of 2.45 kg m^{-2} h^{-1} and brine treatment capacity of 1.43 kg m^{-2} h^{-1}, which is comparable to the results of the pump-driven system (Figure

S10). These results convincingly demonstrate the PME can also work well with the passive water delivery mode.

The quality of the collected water was evaluated. Figure 4c compares the ion concentrations of the feedwater and produced freshwater. As seen, the concentrations of Ca^{2+}, Na^{+}, K^{+} and Mg^{2+} in the collected freshwater (< 4 ppm) decreased by orders of magnitude after desalination by PME, which are much lower than the WHO drinking water standards. All of these results demonstrate that the PME is capable of conveniently achieving highly efficient electricity generation and clean water production under a lower PV temperature.

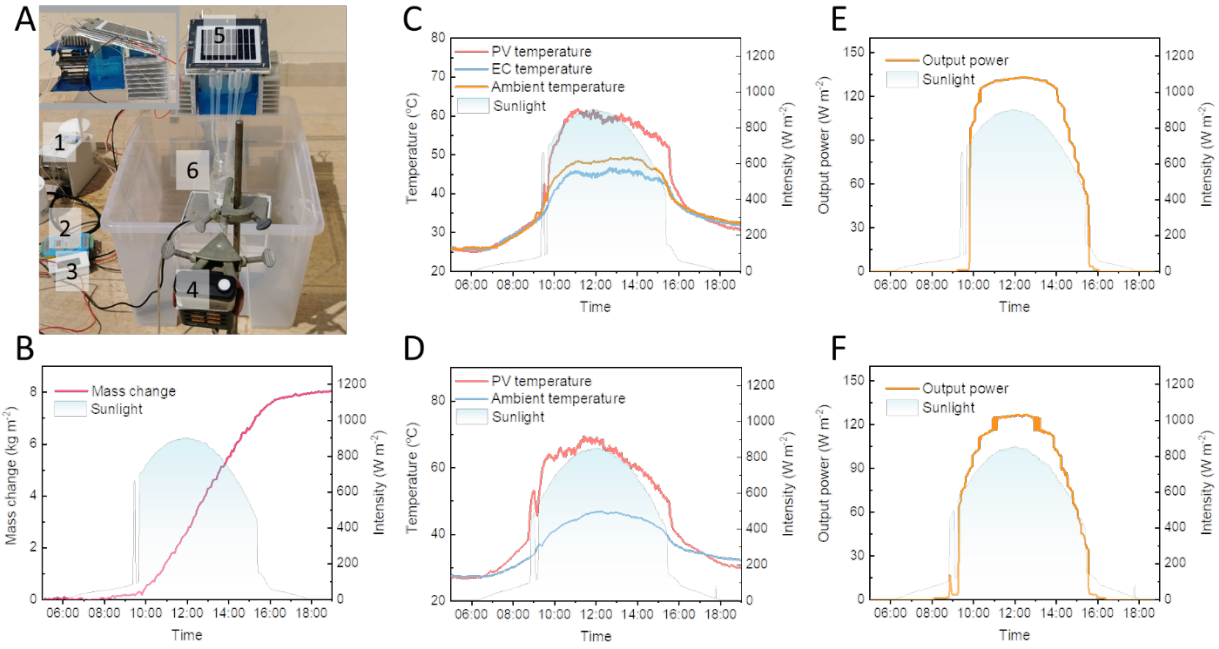

Figure 5. Outdoor experiments of the PME device (solar cell working alone is also measured for comparison). (A) Experimental setup of PME (1 pump; 2 temperature module; 3 coulombmeter; 4 solar irradiation meter; 5 the PME device; 6 produced freshwater container). (B) Mass change of the collected produced water of the PME device and solar irradiation. (C) Temperature evolution of the solar cell in PME and (D) working alone. (E) Output power of the solar cell in the PME and (F) working alone.

Outdoor test. A PME device with a larger sized solar cell of 16x16 cm was fabricated for outdoor experiment in the field (Figure 5a and Figure S11). The device was mounted towards the south at a tilt of 22°. The tests were performed at the balcony of an apartment in KAUST campus between Oct 8~12, 2020. It is worth mentioning that the surrounding ambient temperatures were measured by a thermal couple around 40 cm above the ground and were consistently 5~8°C higher than the ambient temperature reported by the local weather bureau, but it was closer to the environmental temperature of the device. The solar cell was connected to a resistance (50 Ω). The flow rate of the Rea Sea seawater was controlled at 3.0 kg m^{-2} h^{-1} from 9:00 to 17:00 each day. The concentrated brine was directly discharged into the source water container of the EC and 300 g of seawater was added to the EC source water container daily before the operation to ensure EC evaporation continuity. As a control, the same solar cell was taken off the PME and its performance was evaluated alone.

The corresponding daily natural solar irradiation was 4.87 kWh m^{-2} for PME test and 4.84 kWh m^{-2} for the sole solar cell test. The wind speed during the experiments in these two days were reported to be similarly 17 km h^{-1}.[44] In other words, these two experiments were performed in similar environmental conditions.

As shown in Figure 5b, the PME device exhibited an impressive water production performance of 8.09 kg m^{-2}·day^{-1} or 1.66 kg m^{-2}·kWh^{-1} based on the measured natural solar irradiation during the experiments. The weight of the buffered seawater was reduced to around 223 g, indicating that zero liquid discharge can be achieved under this condition. The temperature evolutions of the solar cell, EC and ambient air near the device are shown in Figure 5c. Interestingly, the EC exhibited a lower temperature than the ambient air. This should be attributed to the effect of the natural wind in outdoor conditions. It was reported that the wind is capable of promoting evaporation and thus decreasing evaporation surface temperature.[45] Therefore, it is expected that the brine treatment capacity of the EC in the outdoor condition should be higher than the value measured in the lab. With an ambient temperature at 48.2°C, the solar cell in PME showed a maximum temperature of 61.7 °C, having a temperature disparity of only 13.5°C. In comparison, the solar cell alone in the control experiment showed a highest temperature of 69.5°C with an

ambient temperature of 45.6°C, having a temperature disparity of 23.9°C (Figure 5d), which is much higher than that of the solar cell in the PME system.

The electricity generation performances by the solar cell and PME are shown in Figure 5e-f and summarized in Supplementary Table 1. The electricity conversion efficiency of the solar cell in the PME was 13.76%, which represents 2.46% increase from that of the solar cell working alone in the control experiment (13.43%). The PV cooling performance and water production rate were lower than what was achieved in the lab condition, which was mainly caused by the effect of the natural wind. The wind increases thermal convection heat loss of the solar cell, lowers solar cell temperature, and reduces water production rate. However, even under this condition, the PME device still decreased the solar cell temperature by around ~7°C (See more information about practical consideration in Note S6).

To simulate the situation without wind in the outdoor experiments, the solar cell was covered on the top by a transparent cover made by polymethyl methacrylate (PMMA), as shown in Figure S12A. In this case, the corresponding daily natural solar irradiation was 4.97 kWh m^{-2} for PME test and 4.81 kWh m^{-2} for the sole solar cell test. During 12:00~13:00, the temperature of the solar cell in the PME was averaged to be around ~72.9°C, with an ambient temperature of 52.7°C. Whereas the solar cell working alone exhibited an average temperature of 85.9°C with an ambient temperature of 45.5°C (Figure S12B-D). It is noteworthy that some of the incoming solar irradiation was absorbed and reflected by the cover, which explains why the solar cell working with the top cover exhibited a lower electricity conversion efficiency. The electricity conversion efficiency of the solar cell in the PME was 11.27%, representing 8.37% increase from 10.40% of the solar cell alone (Figure S12E-F). These results indicate that PME is capable of highly efficiently producing freshwater, reducing the solar cell temperature and increasing its electricity conversion efficiency at the same time, a task that was never been achieved previously.

DISCUSSION

In PME, the total amount of solar energy absorbed by the solar cell depends on the solar cell's solar absorptance (α) while the amount of electricity generated is related to its electricity conversion efficiency. Given that the solar cell in the PME has a solar absorptance of 0.89 and electricity conversion efficiency of around 14% as presented earlier, the heat generated by the solar cell is thus calculated to be 750 W m^{-2} under one sun illumination. The solar cell is heated up to an equilibrium temperature of ~47°C when the 5-stage PME device is illuminated under one sun according to the experimental results. Some of the heat is lost to the thermal radiation by the solar cell surface, which is calculated to be 124 W m^{-2} using Stefan-Bolzman's law (equation S-2).[46] As a result, the remaining energy available for the MSMD component to desalinate seawater is 626 W m^{-2}. Moreover, the heat loss from the side area of PME should be less a concern. For the device with the size of 1x1 m, the height of a 5-stage MSMD would be less than 2 cm. Moreover, polyurethane (PU) foam, whose thermal conductivity is around 0.022 W m^{-1} K^{-1}, can be utilized to cover the side area for thermal insulation. The heat loss from the side area is calculated to be less than 1.76 W when the thickness of PU foam is 2 cm and the temperature difference between side area and ambient air is 20 °C (equation S3), which is negligible as compared to the input power of 1000 W (See more details of heat loss in Note S7).

Solar-assisted distillation is proposed generally for seawater desalination at centralized scale and, over the past years, it was believed that 3.5% NaCl solution was a valid surrogate for seawater in solar crystallization, which was proven to be incorrect by our previous work.[39] Real seawater is the mixture of various ions. When water is evaporated out of the seawater, NaCl precipitates dominantly due to its largest abundance, forming cubic crystals which have small porosity in their aggregates. $MgSO_4$, when crystallized, fills all the pore spaces among NaCl crystals, forming a compact salt crust layer on the surface of the evaporator. The salt crust layer, once formed, blocks the seawater brine from transporting to the external surface for evaporation, leading to system failure. When NTA is added to the raw seawater, it selectively modifies NaCl crystallization behavior, leading to the formation of dendritic-shaped crystals having much larger pore spaces in their aggregates. In this case, the $MgSO_4$ crystals are unable to completely occupy and clog the enlarged pores of the NaCl crystals, allowing water transport through the pores by capillary effect

414 during the entire process. Therefore, a stable evaporation rate by EC would be resulted in with
415 the addition of NTA in the source seawater.[39]

416 It is known that the diffusion of water vapor through a hydrophobic membrane with different
417 pore size takes place via three mechanisms: Knudsen region, continuum region and transition
418 region.[47; 48] The Knudsen number (K_n), which is defined as the ratio of the mean free path (λ) of
419 the gas to the pore size (d_p), provides a useful guideline in determining which mechanism is
420 applicable inside the membrane pore.[47] In Knudn region where the pore size is smaller than the
421 mean free path, the collision between molecule and the wall is predominant and increasing the
422 pore size of the hydrophobic membrane reduces this collision. As a result, the membrane
423 coefficient, defined as the ratio of the vapor flux to the vapor pressure difference across the
424 membrane (equation S-6), increases with an increase in pore size (Figure S13), which explains a
425 higher water production rate in the theoretical model (Figure S2E). When the pore size is larger
426 than the mean free path (transition region), besides the molecule-pore wall collisions, the
427 collisions among vapor molecules start to take its grip, which increases the resistance of the vapor
428 diffusion and reduces the membrane coefficient (Figure S13).[37] Consequently, when the pore size
429 is slightly larger than the mean free path, a steep drop in the water production rate and sharp
430 increase in the solar cell temperature are resulted in the theoretical model (Figure S2e). Similar
431 modelling results can be also found in conventional membrane distillation literature.[47; 49] The
432 above analyses help us understand why optimized pore size of the hydrophobic membrane is
433 slightly lower than the mean free path of vapor. The optimized pore size of the hydrophobic
434 membrane as predicted by the model was not used in the experimental work here due to
435 practical consideration and further research efforts can be made to prepare hydrophobic
436 membranes with a uniform pore size slightly lower than the mean free path (See more details on
437 the benefits of theoretical model in Note S8).

438 The heat transfers across the hydrophobic membrane via two pathways: thermal conduction and
439 thermal convection (i.e., evaporation-condensation process). Since the thermal convection
440 directly represents the clean water production performance, increasing the thermal convection
441 and reducing the thermal conduction is thus the key to enhancing water production performance.
442 According to equation S-3, S-6 and S-7, to decrease the thermal conduction loss, it needs reduce

the temperature difference and/or increase the thickness of the hydrophobic membrane. On the other hand, an increase in the thermal convection can be from an increase in membrane coefficient or the temperature difference between the evaporation layer and condensation layer. As reducing the thickness of the membrane decreases the membrane's thermal resistance and temperature difference as well as, meanwhile, increase the membrane coefficient, the effect of the membrane thickness on these two thermal transfer pathways is unclear until a theoretical analysis is made by the thermal model. The model predicted temperature difference between the evaporation layer and condensation layer in a 5-stage PME device is shown in Figure S14A. As seen, increasing the membrane thickness increases the temperature difference greatly. Specifically, the overall temperature difference of the 5 stages is increased from 3.4 ^{o}C at a membrane thickness of 0.1 mm to 42.2 ^{o}C at a thickness of 4 mm. Since the membrane coefficient is much higher at a lower membrane thickness (Figure S14B), it makes possible to effectively drive the vapor diffusion by a low temperature difference using a thin membrane. Moreover, when the membrane thickness is increased, the solar cell temperature can be increased greatly. It is noteworthy that the thermal radiation energy loss is a function of T^4. When the membrane thickness is increased from 0.1 mm to 4 mm, the thermal radiation energy loss of the solar cell can be increased by 270 W m^{-2} from ~123 to ~393 W m^{-2} (Figure S14C) while the maximum thermal conduction "loss" is increased only by 136 W m^{-2}, from ~262 to ~126 W m^{-2} (Figure S14D). These results indicate that the reduced thermal radiation energy loss with a thin membrane can overcompensate the thermal conduction loss, leading to an overall higher thermal convection transfer and thus higher clean water production rate.

The theoretical model developed in this work provides a direction for the optimization of solar-assisted MSMD. In the previous multistage membrane distillation reports, a higher clean water production rate was generally achieved by adopting a thick membrane (e.g., 4 mm) or air-gap (e.g. 2.5 mm), as the thermal conduction "loss" was reduced this way. As a result, the top photothermal material in the multistage membrane distillation device showed a very high temperature (e.g., 62^{o}C[19] and 70^{o}C[5]). Assuming regular photothermal materials with an emissivity of 0.93 were used in these reports, the thermal radiation energy loss could be as high as 250 W m^{-2} and 317 W m^{-2} respectively. One may argue that this high thermal radiation energy

loss can be solved by using the photothermal material with a lower emissivity, but, for the solar cell, reducing its emissivity is technically challenging and practically meaningless as working at such a high temperature would reduce its electricity generation efficiency and increase its aging rate. Thus, the modelling and experimental results of this work, which theoretically predicted and experimentally demonstrated that a thinner membrane could result in a higher clean water production rate and lower solar cell temperature, would help clear some confusions, correct the misconception, and serve as a valuable guidance for the field to move forward (See more details on the future perspective of PME in Note S9).

In all, we successfully develop a photovoltaics-membrane distillation-evaporative crystallizer (PME) system where the waste heat of the solar cell is used to produce clean water at an ultrahigh rate and the clean water production in turns helps cool the solar cell, leading to considerable amount of more electricity being produced simultaneously. Notably, in achieving more electricity and high freshwater production from seawater, such a system discharges no liquid waste. This strategy has a potential to make a solid contribution to the global water-energy nexus.

Methods

Materials. The 1 mm thick stainless-steel mesh with the porosity of 82% and pore size of 15 μm used for evaporation and condensation layer was supplied by Furun. The 0.1 mm thick hydrophobic (PTFE) membrane was supplied by Zhejiang Kertice Hi-tech Fluor-material Co., LTD, with the pore size of 1.00 μm and the porosity of 86%. The epoxy glue used to seal the devices was supplied by ALTECO CHEMICAL PTE LTD. The thermal conduction layer and the pipe with the inner diameter of 0.7 mm and outer diameter of 0.9 mm used for water transport were made by 316L stainless steel. The solar cell was provided by Shunfen New Energy and the non-woven fabrics for evaporative crystallizer (EC) was provided by Kimberly-Clark. Seawater was obtained from Red Sea. The scale inhibitor (BT-008) was purchased from Yayi.

Device assembly. The porous stainless-steel mesh was used in the evaporation layer and condensation layer as support. The stainless steel mesh with the size of 40x40 mm and thickness of 1 mm, PTFE hydrophobic membrane with the size of 55x55 mm and 1 mm thick stainless steel sheet with the size of 50x50 mm were firstly assembled as shown in Figure S3. Then two stainless-steel pipes were inserted into the opposite sides of each evaporation layer and 1 stainless-steel pipe was inserted into the other side of the condensation layer. Equal amount resin (A) and hardener (B) of the epoxy glue were mixed thoroughly until a uniform color is achieved and then filled into the empty space between the stainless steel sheet and membrane. The MSMD component was obtained after the glue fully cured (24 h). In addition, as the glue is black, to avoid the photothermal effect of the glue, the glue on the top was covered by white tape. For EC, the non-woven fabrics were cut into the size of 40x150 mm with 3 parts: a tail (40 mm), evaporation center (40 mm) and wick. The evaporation center was glued to the stainless steel as follows: a piece of plastic wrap with the size of 50x50 mm was placed on a piece of stainless steel with the size of 70x70 mm and then the stainless steel was heated up to 180 ^{o}C by a heating platform. After that, the evaporation center part of the cut non-woven fabrics was pressed on the surface of the plastic wrap and kept there for 20 seconds. The PME system was integrated as Figure 1.

Freshwater production and electricity generation evaluation. The experimental setup was made as shown in Figure 3a. The flow rate of the peristaltic pump was calibrated by the electrical balance. Solar irradiation was provided by a solar simulator (Newport 94043A) with a standard AM 1.5 G spectrum optical filter. The produced water was collected by a 100 ml quartz cup and the weight of the collected cup was monitored by an electrical balance. The source water for the EC was contained by another 100 ml glass cup and its weight was monitored by another electrical balance. The temperature of the solar cell, EC and ambient were detected by thermal couples. J-V curve of the solar cell was measured by a Keithley 2400 series source meter. When seawater was used as feedwater, the seawater was firstly pretreated by filtration, and then small amount of NTA and scale inhibitor were added to form a solution with the concentration of 10 ppm and 5 ppm, respectively. In the first cycle, seawater was directly utilized as source water of EC. In the following four cycles, the source water of EC was prepared by mixing small amounts of seawater with the concentrated brine produced from previous cycle (at the ratio of 1:2). The flow rate of the seawater was controlled at 3.5 kg m^{-2} h^{-1} and each cycle was kept at least for 8 hours. After that, the feedwater flow was controlled at 0.3 kg m^{-2} h^{-1} and kept for 12 h in dark.

In the gravity-driven flow mode, a plastic bottle that contained feedwater was specially designed and fabricated as shown in Figure S8 and S9. The bottle was placed about 5 cm higher than the PME device and the outlet of the bottle was connected to the inlet of the PME device by a plastic pipe. The flow rate was controlled by a clip on the pipe and calibrated by the electrical balance. Other experimental conditions were the same as the pump-driven mode.

Characterization. The UV-Vis-NIR diffuse reflectance spectra of the solar cell was measured by an Aglient Cary 5000 spectrometer, with $BaSO_4$ powder as reference. The concentrations of the ions were detected by Inductively Coupled Plasma Optical Emission Spectrometer (ICP-OES).

SUPPLEMENTARY INFORMATION

Supplementary information includes 14 figures and 1 table.

AUTHOR CONTRIBUTIONS

W.W., Y.S. and P.W. designed the experiments. W.W. and S. A. conducted the experiments. W.W., S. A. and C.Z. analyzed data. P.W. and W.W. wrote the paper. All authors commented on the manuscript drafts.

DECLARE OF INTERESTS

The authors declare no competing interests.

REFERENCE

1 Das, D., and Safini, H. (2018). Water insecurity in urban India: Looking through a gendered lens on everyday urban living. Environment and Urbanization ASIA *9*, 178-197.

2 Vikesland, P.J. (2018). Nanosensors for water quality monitoring. Nat. Nanotechnol. *13*, 651-660.

3 WHO (2017). Progress on drinking water, sanitation and hygiene: 2017 update and SDG baselines.

4 Chiavazzo, E., Morciano, M., Viglino, F., Fasano, M., and Asinari, P. (2018). Passive solar high-yield seawater desalination by modular and low-cost distillation. Nat. Sustain. *1*, 763-772.

5 Xu, Z., Zhang, L., Zhao, L., Li, B., Bhatia, B., Wang, C., Wilke, K.L., Song, Y., Labban, O., and Lienhard, J.H. (2020). Ultrahigh-efficiency desalination via a thermally-localized multistage solar still. Energy & Environmental Science *13*, 830-839.

6 Li, Y., Gao, T., Yang, Z., Chen, C., Luo, W., Song, J., Hitz, E., Jia, C., Zhou, Y., and Liu, B. (2017). 3D-printed, all-in-one evaporator for high-efficiency solar steam generation under 1 sun illumination. Adv. Mater. *29*, 1700981.

7 Garg, M.C., and Joshi, H. (2015). A review on PV-RO process: solution to drinking water scarcity due to high salinity in non-electrified rural areas. Sep. Sci. Technol. *50*, 1270-1283.

8 Clemens, M., Khurelbaatar, G., Merz, R., Siebert, C., van Afferden, M., and Rödiger, T. (2020). Groundwater protection under water scarcity; from regional risk assessment to local wastewater treatment solutions in Jordan. Sci. Total Environ. *706*, 136066.

9 Zarzo, D., and Prats, D. (2018). Desalination and energy consumption. What can we expect in the near future? Desalination *427*, 1-9.

10 Zhu, L., Gao, M., Peh, C.K.N., Wang, X., and Ho, G.W. (2018). Self-Contained Monolithic Carbon Sponges for Solar-Driven Interfacial Water Evaporation Distillation and Electricity Generation. Advanced Energy Materials *8*, 1702149.

11 Agency, I.E. (2019). Key World energy Statistics 2019 (IEA Paris).

12 Waheed, R., Chang, D., Sarwar, S., and Chen, W. (2018). Forest, agriculture, renewable energy, and CO_2 emission. J. Clean. Prod. *172*, 4231-4238.

13 Giannakis, E., Serghides, D., Dimitriou, S., and Zittis, G. (2020). Land transport CO_2 emissions and climate change: evidence from Cyprus. Int. J. Sustain. Energy, 1-14.

14 Partanen, A.-I., Leduc, M., and Matthews, H.D. (2017). Seasonal climate change patterns due to cumulative CO_2 emissions. Environ. Res. Lett. *12*, 075002.

15 Stylos, N., and Koroneos, C. (2014). Carbon footprint of polycrystalline photovoltaic systems. J. Clean. Prod. *64*, 639-645.

16 Nugent, D., and Sovacool, B.K. (2014). Assessing the lifecycle greenhouse gas emissions from solar PV and wind energy: A critical meta-survey. Energy Policy *65*, 229-244.

17 Jäger-Waldau, A. (2019). PV status report 2019, EUR 29938 EN. Publications Office of the European Union, Luxembourg.

18 Rühle, S. (2016). Tabulated values of the Shockley–Queisser limit for single junction solar cells. Solar Energy *130*, 139-147.

19 Wang, W., Shi, Y., Zhang, C., Hong, S., Shi, L., Chang, J., Li, R., Jin, Y., Ong, C., and Zhuo, S. (2019). Simultaneous production of fresh water and electricity via multistage solar photovoltaic membrane distillation. Nature communications *10*, 1-9.

20 Li, R., Shi, Y., Wu, M., Hong, S., and Wang, P. (2020). Photovoltaic panel cooling by atmospheric water sorption–evaporation cycle. Nat. Sustain., 1-8.

21 Makki, A., Omer, S., and Sabir, H. (2015). Advancements in hybrid photovoltaic systems for enhanced solar cells performance. Renew. Sust. Energ. Rev. *41*, 658-684.

22 Sargunanathan, S., Elango, A., and Mohideen, S.T. (2016). Performance enhancement of solar photovoltaic cells using effective cooling methods: A review. Renewable and Sustainable Energy Reviews *64*, 382-393.

23 Dubey, S., Sarvaiya, J.N., and Seshadri, B. (2013). Temperature dependent photovoltaic (PV) efficiency and its effect on PV production in the world–a review. Energy Procedia *33*, 311-321.

24 Fesharaki, V.J., Dehghani, M., Fesharaki, J.J., and Tavasoli, H. (2011). The effect of temperature on photovoltaic cell efficiency. Paper presented at: Proceedings of the 1st International Conference on Emerging Trends in Energy Conservation–ETEC, Tehran, Iran.

25 Skoplaki, E., and Palyvos, J.A. (2009). On the temperature dependence of photovoltaic module electrical performance: A review of efficiency/power correlations. Sol. Energy *83*, 614-624.

26 Hasanuzzaman, M., Malek, A., Islam, M., Pandey, A., and Rahim, N. (2016). Global advancement of cooling technologies for PV systems: A review. Sol. Energy *137*, 25-45.

27 LaPotin, A., Zhong, Y., Zhang, L., Zhao, L., Leroy, A., Kim, H., Rao, S.R., and Wang, E.N. (2020). Dual-Stage Atmospheric Water Harvesting Device for Scalable Solar-Driven Water Production. Joule.

28 Xu, N., Zhu, P., Sheng, Y., Zhou, L., Li, X., Tan, H., Zhu, S., and Zhu, J. (2020). Synergistic Tandem Solar Electricity-Water Generators. Joule *4*, 347-358.

29 Ortigara, A.R.C., Kay, M., and Uhlenbrook, S. (2018). A review of the SDG 6 synthesis report 2018 from an education, training, and research perspective. Water *10*, 1353.

30 McCollum, D., Gomez Echeverri, L., Riahi, K., and Parkinson, S. (2017). SDG 7: Ensure access to affordable, reliable, sustainable and modern energy for all.

31 Montgomery, R. (1947). Viscosity and thermal conductivity of air and diffusivity of water vapor in air. Journal of Meteorology *4*, 193-196.

32 Phattaranawik, J., Jiraratananon, R., and Fane, A. (2003). Effect of pore size distribution and air flux on mass transport in direct contact membrane distillation. J. Membr. Sci. *215*, 75-85.

33 Price, D.M., and Jarratt, M. (2002). Thermal conductivity of PTFE and PTFE composites. Thermochim. Acta *392*, 231-236.

34 Smallwood, I. (2012). Handbook of organic solvent properties (Butterworth-Heinemann).

35 Srisurichan, S., Jiraratananon, R., and Fane, A. (2006). Mass transfer mechanisms and transport resistances in direct contact membrane distillation process. J. Membr. Sci. *277*, 186-194.

36 Horseman, T., Su, C., Christie, K.S., and Lin, S. (2019). Highly effective scaling mitigation in membrane distillation using a superhydrophobic membrane with gas purging. Environmental Science & Technology Letters *6*, 423-429.

37 Khayet, M., Velázquez, A., and Mengual, J.I. (2004). Modelling mass transport through a porous partition: effect of pore size distribution. Journal of non-equilibrium thermodynamics *29*, 279-299.

38 Shi, Y., Zhang, C., Li, R., Zhuo, S., Jin, Y., Shi, L., Hong, S., Chang, J., Ong, C., and Wang, P. (2018). Solar Evaporator with Controlled Salt Precipitation for Zero Liquid Discharge Desalination. Environmental science & technology *52*, 11822-11830.

39 Zhang, C., Shi, Y., Shi, L., Li, H., Li, R., Hong, S., Zhuo, S., Zhang, T., and Wang, P. (2021). Designing a next generation solar crystallizer for real seawater brine treatment with zero liquid discharge. Nat. Commun. *12*, 1-10.

40 Khan, M.A.S., Singh, A., Haldar, S., and Ganguly, B. (2011). Can nitrilotriacetic acid (NTA) act as a habit modifier for rock salt crystals? an answer from computational and experimental studies. Cryst. Growth Des. *11*, 1675-1682.

41 Anderson, R.L., Bishop, W.E., Campbell, R.L., and Becking, G.C. (1985). A review of the environmental and mammalian toxicology of nitrilotriacetic acid. CRC Crit. Rev. Toxicol. *15*, 1-102.

42 Shi, Y., Li, R., Jin, Y., Zhuo, S., Shi, L., Chang, J., Hong, S., Ng, K.-C., and Wang, P. (2018). A 3D photothermal structure toward improved energy efficiency in solar steam generation. Joule *2*, 1171-1186.

43 Mazer, J.A. (1996). Solar cells: an introduction to crystalline photovoltaic technology (Kluwer Academic Publishers Boston).

44 Past Weather in Thuwal, Saudi Arabia — Yesterday and Last 2 Weeks. https://www.timeanddate.com/weather/@409682/historic (accessed Oct. 25).

45 Li, J., Wang, X., Lin, Z., Xu, N., Li, X., Liang, J., Zhao, W., Lin, R., Zhu, B., and Liu, G. (2020). Over 10 kg m^{-2} h^{-1} evaporation rate enabled by a 3D interconnected porous carbon foam. Joule *4*, 928-937.

46 Montambaux, G. (2018). Generalized Stefan–Boltzmann law. Found. Phys. *48*, 395-410.

47 Alkhudhiri, A., Darwish, N., and Hilal, N. (2012). Membrane distillation: A comprehensive review. Desalination *287*, 2-18.

48 Ding, Z., Ma, R., and Fane, A. (2003). A new model for mass transfer in direct contact membrane distillation. Desalination *151*, 217-227.

49 Qtaishat, M.R. (2006). Design of novel direct contact membrane distillation membranes. Desalination *192*, 105-111.

655

656

657